GEOLOGY | THE GEOLOGICAL SOCIETY OF AMERICA®

https://doi.org/10.1130/G50493.1

Manuscript received 27 November 2021
Revised manuscript received 10 June 2022
Manuscript accepted 7 July 2022

Published online 20 October 2022

High-magnitude stresses induced by mineral-hydration reactions

Oliver Plümper[1]*, David Wallis[1,2], Floris Teuling[1], Evangelos Moulas[3], Stefan M. Schmalholz[4], Hamed Amiri[1] and Thomas Müller[5]

[1]Department of Earth Sciences, Utrecht University, 3584 CB Utrecht, Netherlands
[2]Department of Earth Sciences, University of Cambridge, Cambridge CB2 3EQ, UK
[3]Institute of Geosciences, Johannes Gutenberg Universität Mainz, 55099 Mainz, Germany
[4]Institute of Earth Sciences, University of Lausanne, CH-1015 Lausanne, Switzerland
[5]Department of Mineralogy, Georg-August-Universität Göttingen, 37073 Göttingen, Germany

ABSTRACT

Fluid-rock interactions play a critical role in Earth's lithosphere and environmental subsurface systems. In the absence of chemical mass transport, mineral-hydration reactions would be accompanied by a solid-volume increase that may induce differential stresses and associated reaction-induced deformation processes, such as dilatant fracturing to increase fluid permeability. However, the magnitudes of stresses that manifest in natural systems remain poorly constrained. We used optical and electron microscopy to show that one of the simplest hydration reactions in nature [$MgO + H_2O = Mg(OH)_2$] can induce stresses of several hundred megapascals, with local stresses of as much as ~1.5 GPa. We demonstrate that these stresses not only cause fracturing but also induce plastic deformation with dislocation densities (10^{15} m^{-2}) exceeding those typical of tectonically deformed rocks. If these reaction-induced stresses can be transmitted across larger length scales, they may influence the bulk stress state of reacting regions. Moreover, the structural damage induced may be the first step toward catastrophic rock failure, triggering crustal seismicity.

INTRODUCTION

When fluids infiltrate rocks, resultant mineral reactions modify physicochemical rock properties, having a first-order effect on geodynamic and geochemical processes within the lithosphere. These fluid-driven mineral reactions may govern, e.g., the stability of the lithosphere (Jackson et al., 2004; Hilairet et al., 2007), the formation of ore deposits (e.g., Sillitoe, 2010), and environmental subsurface processes such as the sequestration of anthropogenic CO_2 (e.g., Matter et al., 2016). For more than a century, scientists have argued whether fluid-rock interactions occur at constant solid volume or are accompanied by solid-volume changes, ΔV_s, with immediate implications for element mobility and the generation of differential stress (Lindgren, 1918; Carmichael, 1987; Fletcher and Merino, 2001; Wheeler, 2020).

While fluid-driven mineral-replacement reactions can occur without substantial positive ΔV_s (Plümper et al., 2017), observations of natural rocks and laboratory experiments reveal that mineral reactions involving an increase in solid volume in a confined space can generate differential stresses on the confining boundaries (e.g., Jamtveit et al., 2009; Kelemen and Hirth, 2012; Plümper et al., 2012; Zheng et al., 2018). This phenomenon is known as the "force of crystallization" (Becker and Day, 1905). More recently, this process has received increased interest because it may explain the widespread alteration of mantle peridotite (Rudge et al., 2010; Plümper et al., 2012), having implications for deep volatile cycles and the sequestration of CO_2 (Kelemen and Matter, 2008). Moreover, variation in local normal stresses during mineral reaction may have consequences for the thermodynamics of the reaction (Wheeler, 2020).

Although efforts have been made to quantify the magnitudes of stresses that can be exerted during mineral growth, theoretical predictions of differential stresses exceeding 1 GPa (Kelemen and Hirth, 2012; Wolterbeek et al., 2018), experimental constraints of 20–160 MPa (Skarbek et al., 2018; Wolterbeek et al., 2018; Zheng et al., 2018), and inferences of stresses $\leq$300 MPa in natural rocks (Kelemen and Hirth, 2012) vary widely. An argument that has been put forward that may explain the limitation of reaction-induced stresses is the healing of grain contacts (Wolterbeek et al., 2018) and the expulsion of the interfacial fluid film (Zheng et al., 2018; Guren et al., 2021) ceasing the reaction. Investigations of stress-relaxation mechanisms have largely focused on brittle fracturing (Jamtveit et al., 2009; Kelemen and Hirth, 2012; Plümper et al., 2012). However, mineral reactions could also induce many other elastic and inelastic deformation processes.

We present an integrated observational and modeling approach to assess the magnitude of reaction-induced stresses generated during one of the simplest mineral-hydration reactions in nature:

$$MgO + H_2O \leftrightarrow Mg(OH)_2. \quad (1)$$

The results show that differential stresses locally reach gigapascal levels and that these stresses induce numerous elastic and inelastic deformation processes in the encompassing marble. Furthermore, pore-network modeling suggests that reaction-induced fracturing increases permeability by several orders of magnitude.

GEOLOGICAL SETTING AND METHODS

The samples investigated here are part of the contact aureole of the Adamello massif,

*E-mail: o.plumper@uu.nl

CITATION: Plümper, O., et al., 2022, High-magnitude stresses induced by mineral-hydration reactions: Geology, v. 50, p. 1351–1355, https://doi.org/10.1130/G50493.1

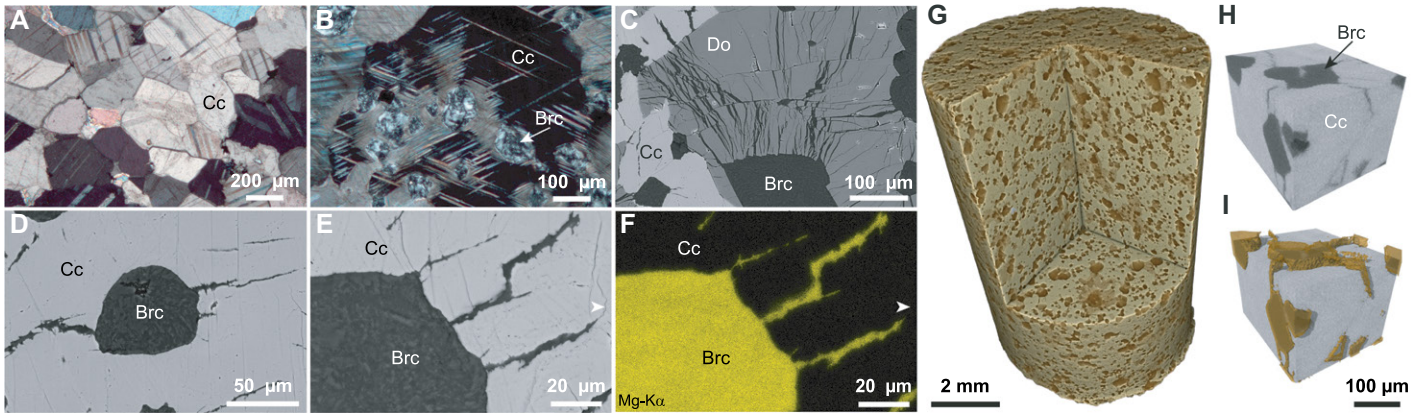

Figure 1. Microstructures within brucite-free and brucite-bearing marble. (A) Marble devoid of brucite (Brc) with low twin density. (B) Marble with high twin density in calcite (Cc) surrounding brucite. (C–D) Cracks emerging from brucite penetrating dolomite (Do) and calcite. (E–F) Cracks are only partially filled with brucite as illustrated in the energy-dispersive X-ray (EDX) map of Mg in F. (G–I) X-ray tomography visualization showing brucite domains and connecting cracks. (H) Magnified view of brucite domains with cracks (dark gray) within calcite (light gray) taken from a representative volume in G, where the solid color is calcite and voids represent brucite and cracks. (I) Segmented brucite shown in brown, highlighting the connectivity of the domains via the crack network. A and B are optical polarization microscope images and C–E are backscattered electron (BSE) images.

Italy (Müller et al., 2009; see the Supplemental Material[1]). The aureole developed within marbles where hydrothermal alteration caused dolomite decomposition into periclase and calcite at ~600 °C. Subsequent hydration resulted in Reaction 1 and an associated positive ΔV_s of as much as 119%. Balancing Reaction 1 at constant volume requires the removal of 54% MgO (see the Supplemental Material). In turn, Mg transport away from the hydration sites would likely trigger the formation of new dolomite, massive brucite precipitation in cracks, or considerable Mg-metasomatic effects within the vicinity of the contact aureole. None of these products were observed.

The carbonate-silicate phase assemblages formed during contact metamorphism suggest a thermodynamic pressure of ~100 MPa (Müller et al., 2009). Estimates of maximum pressures in the Adamello massif are ≤350 MPa (see the Supplemental Material).

We analyzed the marbles using optical, electron, and X-ray microscopy (see the Supplemental Material). Calcite domains around periclase-to-brucite hydration sites were investigated using high-angular-resolution electron backscatter diffraction (HR-EBSD; Wallis et al., 2019). This image cross-correlation technique allows simultaneous mapping of lattice rotations and elastic-strain heterogeneities. The lattice rotations and residual elastic strains can be related to the densities of geometrically necessary dislocations (GNDs; ρ_{GND}) and residual stresses, respectively.

[1]Supplemental Material. High-magnitude, reaction-induced stresses. Please visit https://doi.org/10.1130/GEOL.S.20669139 to access the supplemental material, and contact editing@geosociety.org with any questions. Data are freely available at https://public.yoda.uu.nl/geo/UU01/Z7A6R8.html.

MICROSTRUCTURES

We defined two types of microstructures within the samples: (1) a "background microstructure" (BM) without any brucite (Fig. 1A), and (2) a "reaction microstructure" (RM) where brucite domains are abundant on the millimeter scale (Fig. 1B; see the Supplemental Material). The BM is characterized by calcite grains with thin to tabular twins and an average twin density, $\bar{N}$, of 20 ± 15 mm^{-1} (Fig. 1A). Analysis of 20 thin sections shows that ~60% of the calcite encompassing hydration sites exhibits an increase in tapered twinning with $\bar{N} = 295 \pm 41$ mm^{-1} (Fig. 1B; see the Supplemental Material), indicative of deformation (Barber and Wenk, 1979). In ~20% of all investigated hydration sites, encompassing calcite grains exceed their typical birefringence locally (see the Supplemental Material), interpreted to result from high local residual stresses. Also, carbonate grains encompassing hydration sites exhibit extensive fracturing away from the brucite-carbonate interface (Figs. 1C–1E). Comparison between backscattered electron (BSE) images (Fig. 1E) and Mg element maps (Fig. 1F) reveals that cracks are partially filled with brucite (arrowheads in Figs. 1E and 1F), suggesting that Mg-transport distances were limited. X-ray tomography (Figs. 1G–1I) highlights that the cracks connect hydration sites.

Data from HR-EBSD and transmission electron microscopy (TEM) reveal that dislocation densities vary by orders of magnitude among different microstructural domains. Comparison between the BM and RM data sets shows an increase of two orders of magnitude in ρ_{GND} to $10^{15 \pm 0.4}$ m^{-2} within the RM calcite enclosing the hydration sites (Figs. 2A and 2B; top color axis) (see the Supplemental Material). A difference in dislocation density, ρ, is also apparent from TEM observations made within the BM calcite (Fig. 2C; $\rho = 10^{12 \pm 1}$ m^{-2}) versus across the brucite-calcite interface (Fig. 2D; $\rho = 10^{15 \pm 1}$ m^{-2}). Very high lattice distortions within calcite did not allow HR-EBSD to determine ρ_{GND} directly at the brucite-calcite interface (white areas in Figs. 2A and 2B). However, ρ_{GND} decays from 10^{15} m^{-2} to background levels of 10^{12} m^{-2} across distances of 50–100 µm, implying that dislocation generation is directly linked to processes that occurred at the brucite-calcite interface.

ESTIMATING REACTION-INDUCED STRESS MAGNITUDES

Using HR-EBSD, we determined "present-day" residual stresses from the elastic strains and also used ρ_{GND} to deduce "past" differential stress, σ_d, via the calcite dislocation-density piezometer (De Bresser, 1996; Figs. 2A and 2B, bottom color axis) (see the Supplemental Material):

$$\sigma_d = 10^{-6.21(\pm 0.86)} \rho^{0.62(\pm 0.07)}. \quad (2)$$

We note that the dislocation-piezometer applies to calcite undergoing transient creep at low strains as well as steady-state flow (De Bresser, 1996, his figure 7). Correcting for background differential stress (95 MPa; see the Supplemental Material) results in a minimum σ_d around the hydration sites of 120–220 MPa with local maxima of as much as ~1.5 GPa. These estimates of σ_d are lower bounds because HR-EBSD detects neither (1) orientation gradients in the direction normal to the specimen surface that may result from additional GNDs, nor (2) statistically stored dislocations with lattice-curvature effects that cancel each other out.

We used the twin (Rybacki et al., 2013) and crack (Kelemen and Hirth, 2012) densities observed (Fig. 1; see the Supplemental Material) to estimate the differential-stress magnitudes via the relationships

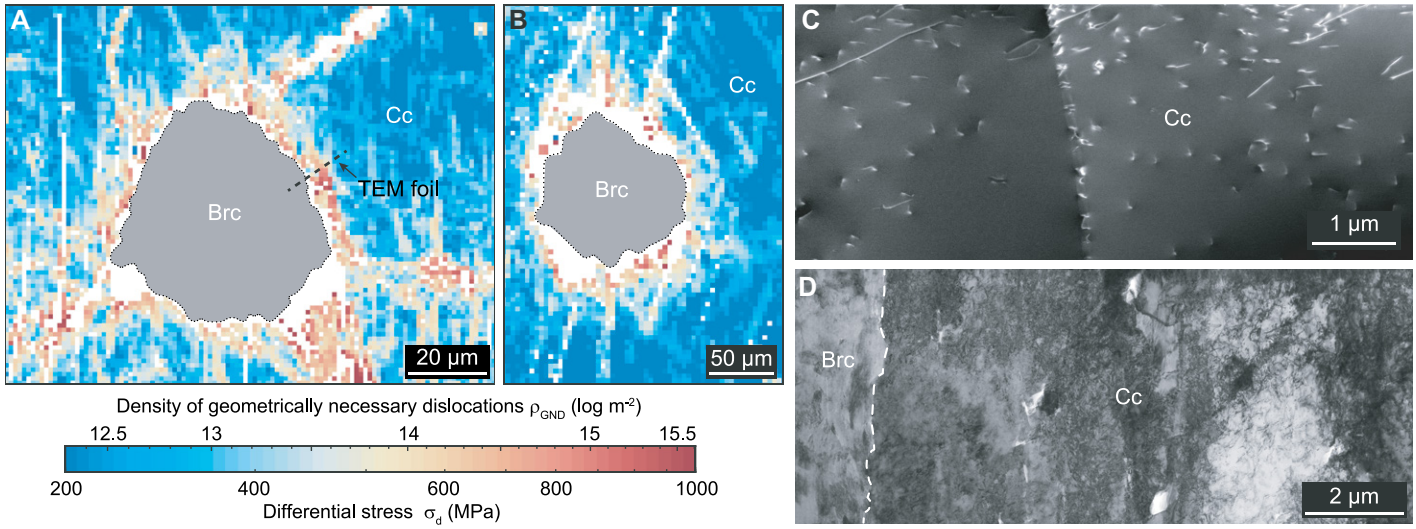

Figure 2. Inelastic deformation and differential stress magnitude around brucite (Brc) domains. Cc—calcite. (A,B) High-angular-resolution electron backscatter diffraction (HR-EBSD) maps of the density of geometrically necessary dislocations (ρ_{GND}) and estimated stresses (De Bresser 1996). (C,D) Transmission electron microscopy (TEM) and scanning TEM (STEM) images depicting the difference in dislocation density ρ between background microstructure (BM) (C) and reaction microstructure (RM) (D) (black dashed line in A; see the Supplemental Material [see footnote 1]).

$$\log(\sigma_t) = (1.29 \pm 0.02) + (0.50 \pm 0.05)\log(N), \quad (3)$$

and

$$\sigma_c \sqrt{\frac{4Y\gamma}{\omega}}, \quad (4)$$

Where σ_t and σ_c are the stresses associated to twinning and fracturing, respectively, Y is the Young's modulus (70 GPa), γ is the surface energy, and ω is the crack spacing within calcite. Measurements of N and ω result in $\sigma_t = 280^{+120}_{-30}$ MPa and $\sigma_c = 760 \pm 150$ MPa ($\gamma = 0.15$ J m^{-2}) to $\sigma_c = 1100 \pm 220$ MPa ($\gamma = 0.32$ J m^{-2}). The variation in σ_c arises from the variability of γ with varying degrees of surface coverage by aqueous fluids (Røyne et al., 2011).

The positive ΔV_s during Reaction 1 may not be the only cause of stress at the brucite-calcite interface. All "host-inclusion" systems that experience pressure-temperature (*P-T*) changes develop pressure differences between the host and inclusion due to differences in elastic properties and thermal expansivities. The only exception is when the system follows an isomeke line, that is, a line in *P-T* space where the volumetric deformation of the inclusion is accommodated by the deformation of its host (Angel et al., 2015). Because this path is unique, any other change in *P-T* would induce a pressure difference between brucite and calcite (Moulas et al., 2020). For the case of isobaric cooling during contact metamorphism, the pressure of the host mineral can be approximated as constant and the developing stresses are controlled by differential thermal expansion. Using a linear-elastic approximation (Supplemental Material), we calculated the potential pressure (mean stress) difference due to cooling from 700 °C (equilibrium periclase-to-brucite temperature at 350 MPa) to 25 °C. The calculation indicates that an "underpressure" of −300 MPa would develop (i.e., thermal contraction of brucite results in a negative pressure difference between brucite and calcite; Supplemental Material). However, reaction-induced cracks emanate radially, whereas negative pressures within the brucite would result in concentric crack patterns (Van der Molen and Van Roermund, 1986).

Overall, we suggest that the differential stresses obtained via the dislocation-density piezometer, twin piezometer, and crack analysis result from the positive ΔV_s during Reaction 1 under confinement within the marble. To further constrain the reaction-induced stress magnitudes, we used a continuum mechanics model for viscoelastic pressure relaxation within a host-inclusion configuration (Dabrowski et al., 2015; see the Supplemental Material). Differential stresses obtained via the dislocation-density piezometer (Fig. 2) show a best fit with the numerical model at ~325 MPa at the brucite-calcite interface (Fig. 3). The model also predicts an effective stress exponent *n* between 2 and 3 in a power-law viscous flow law, consistent with dislocation creep in the host matrix and, therefore, with the observed microstructures.

In summary, differential-stress magnitudes imposed onto the brucite-calcite interface were at least 300 MPa with local stresses of as much as ~1.5 GPa. Moreover, these elevated stresses suggest that if fracturing occurred concomi-

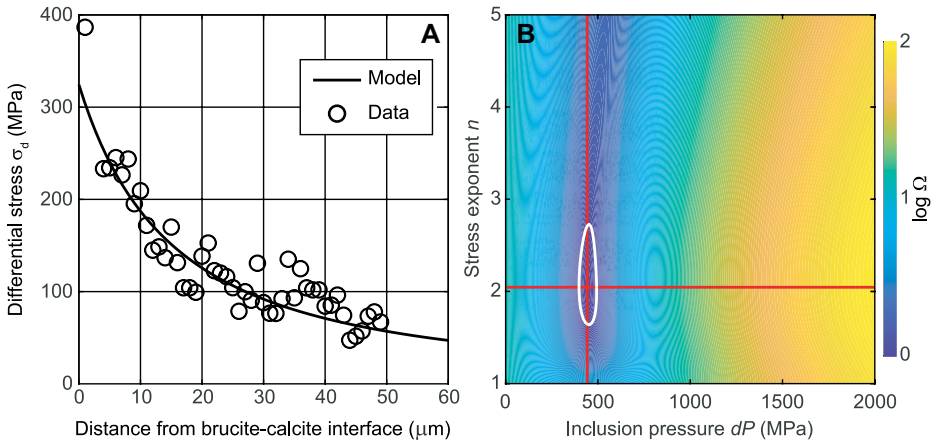

Figure 3. Continuum mechanics model. (A) Best fit of "Dabrowski model" (Dabrowski et al., 2015) to differential stresses obtained via dislocation-density piezometer (De Bresser, 1996) (σ_d; Fig. 2A). (B) Model parameter space, where white contour is 1% confidence interval of cost (or misfit) function Ω between analytical solution and σ_d (Supplemental Material [see footnote 1]).

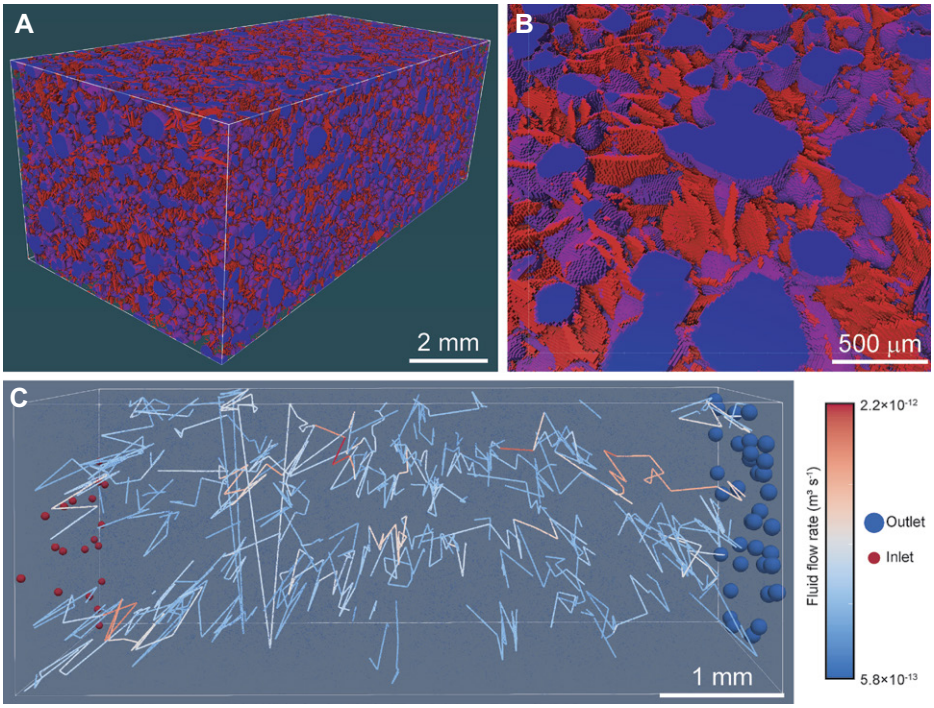

Figure 4. Reaction-induced crack network. (A,B) Crack-network visualization (X-ray tomography; blue indicates brucite domains; red indicates reaction-induced cracks). (C) Corresponding pore-network model and the computation of flow rate from which permeability is determined (see the Supplemental Material [see footnote 1]; Raoof et al., 2013). The model assumes that porous medium can be represented as a network of pore bodies and throats.

tantly with dislocation motion and twinning, it did not fully release the growing reaction-induced stresses.

PARTITIONING AND STORAGE OF REACTION-INDUCED STRAIN ENERGY

Work, *W,* must be done on the environment to accommodate the periclase-to-brucite volume change in the host matrix. Based on the microstructural observations, some of this work has gone into dislocation formation, reaction-induced fracturing, mechanical twinning, and elastic strain (see the Supplemental Material). Hence, we can express *W* as

$$W > E_{\text{dislocation}} + E_{\text{fracture}} + E_{\text{twinning}} + E_{\text{elastic}}, \quad (5)$$

where $E_{\text{dislocation}}$, E_{fracture}, E_{twinning}, and E_{elastic} are the energies associated with the aforementioned processes. Assuming that the energy required during dislocation formation is equal to the currently stored total strain energy around the dislocations (Anderson et al., 2017) and neglecting energy dissipation through heat and acoustic emission upon dislocation motion, we estimate a mean $E_{\text{dislocation}} = 20 \pm 10$ J mol^{-1}. Using experimentally and theoretically determined surface and twin energies, as well as assuming a linear elastic behavior (see the Supplemental Material), we also infer $E_{\text{fracture}} = 1.0 \pm 0.5$ J mol^{-1}, $E_{\text{twinning}} = 16 \pm 2$ J mol^{-1}, and $E_{\text{elastic}} = 335 \pm 125$ J mol^{-1}. These estimates demonstrate that dislocation formation and glide (albeit not specifically considered) were the most prominent inelastic deformation processes induced by Reaction 1. However, most strain energy is stored elastically, although E_{elastic} is likely an overestimate due to the contribution of local strain fields around dislocations within the HR-EBSD maps.

In addition to the aforementioned processes, increased elastic strain within the calcite and, foremost, a locally high reaction-induced normal stress, σ_n, would promote pressure solution of calcite. Following Wheeler et al. (2020), it is evident that the crystal activity of calcite, Δa, is significantly impacted by σ_n via

$$\Delta a = \exp\left(E_i + \frac{[\sigma_n \times V_m]}{RT} \right),$$

where E_i is either $E_{\text{dislocation}}$ or E_{elastic}, V_m is the molar volume of calcite, and R is the gas constant. The preservation of high dislocation densities, elastic strain, twins, and cracks within calcite that can be directly associated to Reaction 1 imply that pressure solution of calcite was minor. Also, pressure solution may have been limited due to a severe reduction in interfacial fluid film thickness, hence decreased water diffusivity (Guren et al., 2021) along the calcite-brucite interface, or due to a strong chemical potential gradient toward the periclase-brucite reaction interface limiting the amount of fluid at the calcite-brucite interface. Nevertheless, complete periclase hydration is evident in all samples, implying that fluid penetrated to the periclase-brucite reaction front, at least over geological time scales.

REACTION-INDUCED FRACTURING AND PERMEABILITY ENHANCEMENT

Using pore-network modeling (Raoof et al., 2013), we estimated the fluid permeability through the reaction-induced crack network obtained via X-ray tomography (Fig. 4; see the Supplemental Material). Assuming that the network was transiently transmissive to aqueous fluids, we computed the volumetric flow rate (Fig. 4C) to obtain a permeability of 0.5×10^{-14} m^2. This computed core-scale permeability is five to six orders of magnitude higher than measurements on intact core-scale marbles (Fischer and Paterson, 1992) and agrees with the permeability-depth relationship of Ingebritsen and Manning (2010) for metamorphically disturbed rocks ($1 \times 10^{-13.3}$ to $1 \times 10^{-14.5}$ m^2 at the depth of contact metamorphism).

CONCLUSIONS

Our observations of one of the simplest natural mineral-hydration reactions show that reaction-induced stresses within rocks can locally reach gigapascal levels. Hence, volume-changing reactions can (1) exert high-magnitude differential stresses onto their surrounding matrix, resulting in deviations from lithostatic pressure, and (2) induce a multitude of irreversible deformation processes with, among others, implications for the transient fluid permeability of the lithosphere. If these reaction-induced stresses can be transmitted across larger length scales, they may influence lithospheric processes, and the induced microscopic damage may be the first step toward catastrophic rock failure, triggering crustal seismicity akin to stress transfer in dehydrating systems (Ferrand et al., 2017).

ACKNOWLEDGMENTS

We thank S. Llana-Fúnez, L. Menegon, and J. Wheeler for their reviews. O. Plümper, F. Teuling, and H. Amiri acknowledge a European Research Council Starting grant (852069) and an Olaf Schuiling Fund (Utrecht University). E. Moulas acknowledges Johannes Gutenberg Universität Mainz.

REFERENCES CITED

Anderson, P.M., Hirth, J.P., and Lothe, J., 2017, Theory of Dislocations (third edition): New York, Cambridge University Press, 718 p.

Angel, R.J., Nimis, P., Mazzucchelli, M.L., Alvaro, M., and Nestola, F., 2015, How large are departures from lithostatic pressure?: Constraints from host–inclusion elasticity: Journal of Metamorphic Geology, v. 33, p. 801–813, https://doi.org/10.1111/jmg.12138.

Barber, D.J., and Wenk, H.-R., 1979, Deformation twinning in calcite, dolomite, and other rhombohedral carbonates: Physics and Chemistry of Minerals, v. 5, p. 141–165, https://doi.org/10.1007/BF00307550.

Becker, G.F., and Day, A.L., 1905, The linear force of growing crystals: Proceedings of the Washington Academy of Sciences, v. 7, p. 283–288.

Carmichael, D.M., 1987, Induced stress and secondary mass transfer: Thermodynamic basis for the tendency toward constant-volume constraint in diffusion metasomatism, *in* Helgeson, H.C., ed., Chemical Transport in Metasomatic Processes: Dordrecht, Springer, p. 239–264, https://doi.org/10.1007/978-94-009-4013-0_10.

Dabrowski, M., Powell, R., and Podladchikov, Y., 2015, Viscous relaxation of grain-scale pressure variations: Journal of Metamorphic Geology, v. 33, p. 859–868, https://doi.org/10.1111/jmg.12142.

De Bresser, J., 1996, Steady state dislocation densities in experimentally deformed calcite materials: Single crystals versus polycrystals: Journal of Geophysical Research, v. 101, p. 22,189–22,201, https://doi.org/10.1029/96JB01759.

Ferrand, T. P., Hilairet, N., Incel, S., Deldicque, D., Labrousse, L., Gasc, J., Renner J., Wang Y., Green II, H.W., and Schubnel, A., 2017, Dehydration-driven stress transfer triggers intermediate-depth earthquakes: Nature Communications, v. 8, p. 1–11, https://doi.org/10.1038/ncomms15247.

Fischer, G.J., and Paterson, M.S., 1992, Measurement of permeability and storage capacity in rocks during deformation at high temperature and pressure, *in* Evans, B., and Wong, T.F., eds., Fault Mechanics and Transport Properties of Rocks: A Festschrift in Honor of W.F. Brace: London, Academic Press, International Geophysics, v. 51, p. 213–252, https://doi.org/10.1016/S0074-6142(08)62824-7.

Fletcher, R.C., and Merino, E., 2001, Mineral growth in rocks: Kinetic-rheological models of replacement, vein formation, and syntectonic crystallization: Geochimica et Cosmochimica Acta, v. 65, p. 3733–3748, https://doi.org/10.1016/S0016-7037(01)00726-8.

Guren, M.G., Sveinsson, H.A., Hafreager, A., Jamtveit, B., Malthe-Sørenssen, A., and Renard, F., 2021, Molecular dynamics study of confined water in the periclase-brucite system under conditions of reaction-induced fracturing: Geochimica et Cosmochimica Acta, v. 294, p. 13–27, https://doi.org/10.1016/j.gca.2020.11.016.

Hilairet, N., Reynard, B., Wang, Y.B., Daniel, I., Merkel, S., Nishiyama, N., and Petitgirard, S., 2007, High-pressure creep of serpentine, interseismic deformation, and initiation of subduction: Science, v. 318, p. 1910–1913, https://doi.org/10.1126/science.1148494.

Ingebritsen, S.E., and Manning, C.E., 2010, Permeability of the continental crust: Dynamic variations inferred from seismicity and metamorphism: Geofluids, v. 10, p. 193–205, https://doi.org/10.1111/j.1468-8123.2010.00278.x.

Jackson, J.A., Austrheim, H., McKenzie, D., and Priestley, K., 2004, Metastability, mechanical strength, and the support of mountain belts: Geology, v. 32, p. 625–628, https://doi.org/10.1130/G20397.1.

Jamtveit, B., Putnis, C.V., and Malthe-Sørenssen, A., 2009, Reaction induced fracturing during replacement processes: Contributions to Mineralogy and Petrology, v. 157, p. 127–133, https://doi.org/10.1007/s00410-008-0324-y.

Kelemen, P.B., and Hirth, G., 2012, Reaction-driven cracking during retrograde metamorphism: Olivine hydration and carbonation: Earth and Planetary Science Letters, v. 345–348, p. 81–89, https://doi.org/10.1016/j.epsl.2012.06.018.

Kelemen, P.B., and Matter, J., 2008, In situ carbonation of peridotite for CO_2 storage: Proceedings of the National Academy of Sciences of the United States of America, v. 105, p. 17,295–17,300, https://doi.org/10.1073/pnas.0805794105.

Lindgren, W., 1918, Volume changes in metamorphism: The Journal of Geology, v. 26, p. 542–554, https://doi.org/10.1086/622615.

Matter, J.M., et al., 2016, Rapid carbon mineralization for permanent disposal of anthropogenic carbon dioxide emissions: Science, v. 352, p. 1312–1314, https://doi.org/10.1126/science.aad8132.

Moulas, E., Kostopoulos, D., Podladchikov, Y., Chatzitheodoridis, E., Schenker, F.L., Zingerman, K.M., Pomonis, P., and Tajčmanová, L., 2020, Calculating pressure with elastic geobarometry: A comparison of different elastic solutions with application to a calc-silicate gneiss from the Rhodope Metamorphic Province: Lithos, v. 378–379, 105803, https://doi.org/10.1016/j.lithos.2020.105803.

Müller, T., Baumgartner, L.P., Foster, C.T., Jr., and Bowman, J.R., 2009, Crystal size distribution of periclase in contact metamorphic dolomite marbles from the southern Adamello Massif, Italy: Journal of Petrology, v. 50, p. 451–465, https://doi.org/10.1093/petrology/egp007.

Plümper, O., Røyne, A., Magrasó, A., and Jamtveit, B., 2012, The interface-scale mechanism of reaction-induced fracturing during serpentinization: Geology, v. 40, p. 1103–1106, https://doi.org/10.1130/G33390.1.

Plümper, O., Botan, A., Los, C., Liu, Y., Malthe-Sørenssen, A., and Jamtveit, B., 2017, Fluid-driven metamorphism of the continental crust governed by nanoscale fluid flow: Nature Geoscience, v. 10, p. 685–690, https://doi.org/10.1038/ngeo3009.

Raoof, A., Nick, H.M., Hassanizadeh, S.M., and Spiers, C.J., 2013, PoreFlow: A complex pore-network model for simulation of reactive transport in variably saturated porous media: Computers & Geosciences, v. 61, p. 160–174. https://doi.org/10.1016/j.cageo.2013.08.005.

Røyne, A., Bisschop, J., and Dysthe, D.K., 2011, Experimental investigation of surface energy and subcritical crack growth in calcite: Journal of Geophysical Research, v. 116, B04204, https://doi.org/10.1029/2010JB008033.

Rudge, J.F., Kelemen, P.B., and Spiegelman, M., 2010, A simple model of reaction-induced cracking applied to serpentinization and carbonation of peridotite: Earth and Planetary Science Letters, v. 291, p. 215–227, https://doi.org/10.1016/j.epsl.2010.01.016.

Rybacki, E., Evans, B., Janssen, C., Wirth, R., and Dresen, G., 2013, Influence of stress, temperature, and strain on calcite twins constrained by deformation experiments: Tectonophysics, v. 601, p. 20–36, https://doi.org/10.1016/j.tecto.2013.04.021.

Sillitoe, R.H., 2010, Porphyry copper systems: Economic Geology, v. 105, p. 3–41, https://doi.org/10.2113/gsecongeo.105.1.3.

Skarbek, R.M., Savage, H.M., Kelemen, P.B., and Yancopoulos, D., 2018, Competition between crystallization-induced expansion and creep compaction during gypsum formation, and implications for serpentinization: Journal of Geophysical Research: Solid Earth, v. 123, p. 5372–5393, https://doi.org/10.1029/2017JB015369.

Van der Molen, I., and Van Roermund, H.L.M., 1986, The pressure path of solid inclusions in minerals: The retention of coesite inclusions during uplift: Lithos, v. 19, p. 317–324, https://doi.org/10.1016/0024-4937(86)90030-7.

Wallis, D., Hansen, L.N., Britton, T.B., and Wilkinson, A.J., 2019, High-angular resolution electron backscatter diffraction as a new tool for mapping lattice distortion in geological minerals: Journal of Geophysical Research: Solid Earth, v. 124, p. 6337–6358, https://doi.org/10.1029/2019JB017867.

Wheeler, J., 2020, A unifying basis for the interplay of stress and chemical processes in the Earth: Support from diverse experiments: Contributions to Mineralogy and Petrology, v. 175, 116, https://doi.org/10.1007/s00410-020-01750-9.

Wolterbeek, T.K.T., van Noort, R., and Spiers, C.J., 2018, Reaction-driven casing expansion: Potential for wellbore leakage mitigation: Acta Geotechnica, v. 13, p. 341–366, https://doi.org/10.1007/s11440-017-0533-5.

Zheng, X.J., Cordonnier, B., Zhu, W.L., Renard, F., and Jamtveit, B., 2018, Effects of confinement on reaction-induced fracturing during hydration of periclase: Geochemistry Geophysics Geosystems, v. 19, p. 2661–2672, https://doi.org/10.1029/2017GC007322.

Printed in USA